Research Article

Journal of RAMAN SPECTROSCOPY

Received: 20 January 2009 Accepted: 4 June 2009 Published online in Wiley Interscience: 21 September 2009

(www.interscience.wiley.com) DOI 10.1002/jrs.2448

Tip-enhanced Raman spectroscopy of carbon nanotubes

Luiz Gustavo Cançado,[a*] Achim Hartschuh[b] and Lukas Novotny[a]

This paper presents an overview on the principles of tip-enhanced Raman spectroscopy (TERS). The technique can be used to record Raman images of carbon nanotubes with high spatial resolution. The high resolution is made possible by local enhancement of the incident and scattered fields. The paper also presents some advances on the science of carbon nanotubes generated by TERS, including the observation of local defects, chirality changes, and dopants. Copyright © 2009 John Wiley & Sons, Ltd.

Keywords: TERS; near-field; Raman; carbon nanotubes

Introduction

Raman spectroscopy has been extensively used for the structural characterization of carbon nanotubes, as well as for studying their basic properties.[1] The diameter and chirality of a single-wall nanotube (SWNT) can be uniquely determined by the shift of the radial breathing mode (RBM) occurring in the range 100–400 cm^{-1}.[2,3] The disorder-induced D band ($\sim$1350 cm^{-1}) can be used to detect defects in the nanotube structure,[4] whereas the shape of the tangential stretching G band ($\sim$1590 cm^{-1}) can be used to identify a SWNT as a semiconductor or metallic type.[5] Moreover, due to its resonant nature, Raman scattering of carbon nanotubes can be used to probe not only phonons but also electrons in their one-dimensional (1D) Brillouin zone. The G' band (a two-phonon band at $\sim$2700 cm^{-1} associated with the disorder-induced D band) is very sensitive to changes in the electron energy dispersion of carbon nanotubes, being useful for the detection of dopants in their 1D structure.[6] Specialists are now using Raman scattering to study unusual phenomena associated with electron–phonon coupling in carbon nanotubes such as Kohn anomalies,[7] Peierls transitions,[8] and the breakdown of the adiabatic (Born-Oppenheimer) approximation.[9]

In spite of its enormous importance, the investigation of carbon nanotubes via conventional Raman spectroscopy is limited due to low spatial resolution. As a consequence, the investigation of details on a single-tube level becomes a difficult task for Raman spectroscopists. This is already a practical problem, since the production of nano-electronic devices based on carbon nanotube technology became a recent reality.[1,10] Tip-enhanced Raman spectroscopy (TERS) provides an alternative way to go beyond this barrier by performing spectroscopic imaging with ultra-high spatial resolution.[11–15] In this review paper, an overview on the principles of TERS is presented. It will be shown how this technique can be used in order to obtain Raman images of carbon nanotubes with high spatial resolution mediated by local enhancement of the incident and scattered fields. The paper also summarizes some advances on the science of carbon nanotubes generated by tip-enhanced Raman measurements, including the detection of local defects, chirality changes, and dopants.[6,16–18]

The Diffraction Limit for Spatial Resolution in Optical Microscopy

Since the main objective of TERS is to improve spatial resolution achieved in Raman scattering, it makes sense to start our analysis by reviewing the origin of the diffraction limit in conventional optical microscopy. The spatial resolution Δx of a standard optical microscope is limited by diffraction to roughly (Abbé criterion):[19]

$$\Delta x = \frac{0.61\lambda}{\mathrm{NA}}, \tag{1}$$

where λ is the wavelength of light, and $\mathrm{NA} = n \sin\theta$ is the numerical aperture of the objective lens. Although the NA can be optimized by performing experiments in surrounding media with large index of refraction n, or by engineering objectives with large collection angles θ, conventional microscopes can only achieve resolutions on the order of $\lambda/2$ ($\geq$200 nm).

The spatial resolution limit given by the Abbé criterion was originally obtained by considering the overlap between the paraxial point-spread function of two dipoles with axes perpendicular to the optical axis of a microscope. Similarly, we have the Rayleigh criterion which is based on the geometry of a grating spectrometer.[19] There are, in fact, many different definitions for the spatial resolution limit, followed by some arbitrariness in their concepts. However, all these definitions originate from the same practical fact: conventional optical systems are not able to collect the whole spectrum of spatial frequencies associated with optical fields generated by a light source located in a distance sufficiently far from the detector (far-field regime).

In order to clarify the statement made in the last paragraph, we will introduce here the angular spectrum representation of optical

* Correspondence to: Luiz Gustavo Cançado, University of Rochester, The Institute of Optics, Rochester, New York 14627, USA. E-mail: cancado@optics.rochester.edu

a University of Rochester, The Institute of Optics, Rochester, New York 14627, USA

b Department Chemie und Biochemie and CeNS, Ludwig-Maximilians-Universität München, 81377 München, Germany

Copyright © 2009 John Wiley & Sons, Ltd.

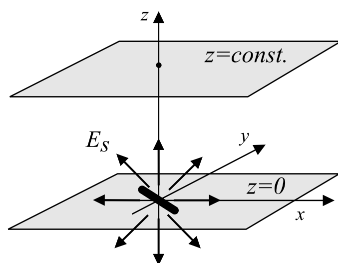

Figure 1. In the angular spectrum representation, the scattered field is evaluated in a plane $z = const$. transverse to an arbitrarily chosen z axis.

fields, which is the series expansion of an arbitrary field in terms of plane and evanescent waves with variable amplitudes and propagation directions (k vectors). Let us consider, for example, the electric field E_s of the inelastically scattered light in a Raman scattering experiment. If we draw an arbitrary z-axis (see Fig. 1), the angular spectrum representation of the electric field E_s in a plane $z = const$. transverse to this axis is given by:[19,20]

$$E_s(x, y, z) = \int \int_{-\infty}^{\infty} \hat{E}_s(k_x, k_y; 0) e^{i(k_x x + k_y y)} e^{\mp i k_z z} dk_x dk_y, \quad (2)$$

where k_x, k_y, and k_z are the spatial frequencies related to the cartesian coordinates x, y, and z, respectively. $\hat{E}_s(k_x, k_y; 0)$ are the Fourier amplitudes of the electric field at $z = 0$.

Let us analyze how the exponential term $e^{\mp i k_z z}$ in Eqn 2 influences the propagation of the electric field E_s along the z-axis. The k-vector (k_x, k_y, k_z) and the frequency $\omega = 2\pi c/\lambda$ are related by the free-space dispersion relation, and hence k_z is given by:

$$k_z = \sqrt{(2\pi n/\lambda)^2 - k_{||}^2}, \quad (3)$$

where we have defined $k_{||}^2 = k_x^2 + k_y^2$. By looking at Eqns 2 and 3 we conclude that for $k_{||} \leq 2\pi n/\lambda$, the wavevector k_z is a real number. In this case, the electric field E_s propagates along the z-axis oscillating with $e^{\mp i k_z z}$, giving rise to the far-field component of the optical field. On the other hand, if $k_{||} > 2\pi n/\lambda$, the wavevector k_z is an imaginary number, and the electric field E_s decays exponentially along the z direction. If the image plane at $z = const$. is sufficiently separated from the source at $z = 0$, the contribution from this decaying part (evanescent waves) will be lost. Therefore, there is always a loss of information from the near field to the far field.

Let us consider now the best case scenario, where the optical field is formed by a sum of plane waves with a Gaussian distribution of spatial frequencies. Because the entire spectrum associated with evanescent fields is lost in the far-field regime, in a position sufficiently far from the source this Gaussian distribution must have a bandwidth $\Delta k_{||} \leq 2\pi n/\lambda$. Since the Fourier transform of a Gaussian distribution with bandwidth $\Delta k_{||}$ is another Gaussian distribution with bandwidth $\Delta r_{||} = 1/\Delta k_{||}$ (we are considering here the uncertainty of a Gaussian function as the square root of its variance), we find that the lateral spatial resolution achieved in the far-field regime cannot be better than $\Delta r_{||} = \lambda/2\pi n$, with $\Delta r_{||} = \sqrt{\Delta x^2 + \Delta y^2}$.

The above scenario gets quite less optimistic if we introduce some reality by considering that we are not able to sample the entire spectrum of $\Delta k_{||}$. In this case, the upper resolution limit will not be defined by the refractive index n, but by the numerical aperture of the collection system, i.e.

$$\Delta r_{||} = \frac{\lambda}{2\pi \mathrm{NA}}. \quad (4)$$

We can see that this lateral resolution limit is, in fact, about 3.8 times higher than the Abbé's limit given in Eqn 1, which is indeed more realistic.[19]

In summary, the spatial resolution limit in far-field optics originates from the fact that evanescent components of the optical field are lost upon propagation. Therefore, to go beyond the diffraction limit requires the detection of the evanescent components of the optical field. Such a trick can actually be done by placing an optical antenna sufficiently near the sample. This is the essence of TERS, which will be discussed in the next section.

The Principles of TERS

The goal of TERS is to obtain the spectral response from nanoscopic structures with optical resolution beyond the diffraction limit. For this purpose, a sharp metal tip is placed sufficiently near the sample surface.[21,22] The tip provides a channel through which the near-field components of the scattered light (evanescent waves) become propagating waves in the far zone. In other words, by using a confined source field with a large bandwidth of spatial frequencies, high spatial frequencies generated from the sample become accessible in the far field, and the spatial resolution is defined by the diameter of the tip apex.[19] However, there is a fundamental issue involved in such an experiment, which is the fact that the signal generated from near-field and far-field components of the scattered light will be intermixed in the far zone. In order to solve this issue, the tip might be able to perform its secondary (but not less important) function: enhance the optical fields generated in the near-field regime.

The field enhancement at the apex of a sharp metal tip can be understood as follows:[19,21,22] the external driving field (which can be the incident or scattered field in a Raman experiment) polarized along the tip axis drives free electrons periodically up and down along the tip shaft with the same frequency as the exciting field. Because of the small surface area near the tip apex, a uniform displacement of the electron sea towards the tip gives rise to a huge surface charge accumulation at the tip end (Fig. 2(a)). These charges generate a secondary field which is seen as the enhanced field at the tip apex (Fig. 2(c)).

Raman scattering is an inelastic process in which incident light of frequency ω_i is converted to scattered light of frequency ω_s, where $\omega_i \neq \omega_s$. For Stokes processes, the frequency of the scattered light is downshifted from the frequency of the incident light by an amount equal to the frequency of the vibrational excitation created in the sample (ω_v), that is, $\omega_s = \omega_i - \omega_v$.[23] In order to achieve the maximum performance in a TERS experiment, it is important to have the enhancement of both the incident and scattered electric fields. For the incident light with frequency ω_i, the field enhancement factor $f(\omega_i)$ is defined as the ratio between the amplitudes of the secondary electric field at the tip apex $E_{tip}(\omega_i)$, and without the tip $E_i(\omega_i)$. Similarly, the field enhancement factor $f(\omega_s)$ for the inelastically scattered light is defined as the ratio $E_{tip}(\omega_s)/E_s(\omega_s)$. Spontaneous Raman scattering is a linear process in which the intensity of the scattered light is linearly

Copyright © 2009 John Wiley & Sons, Ltd.

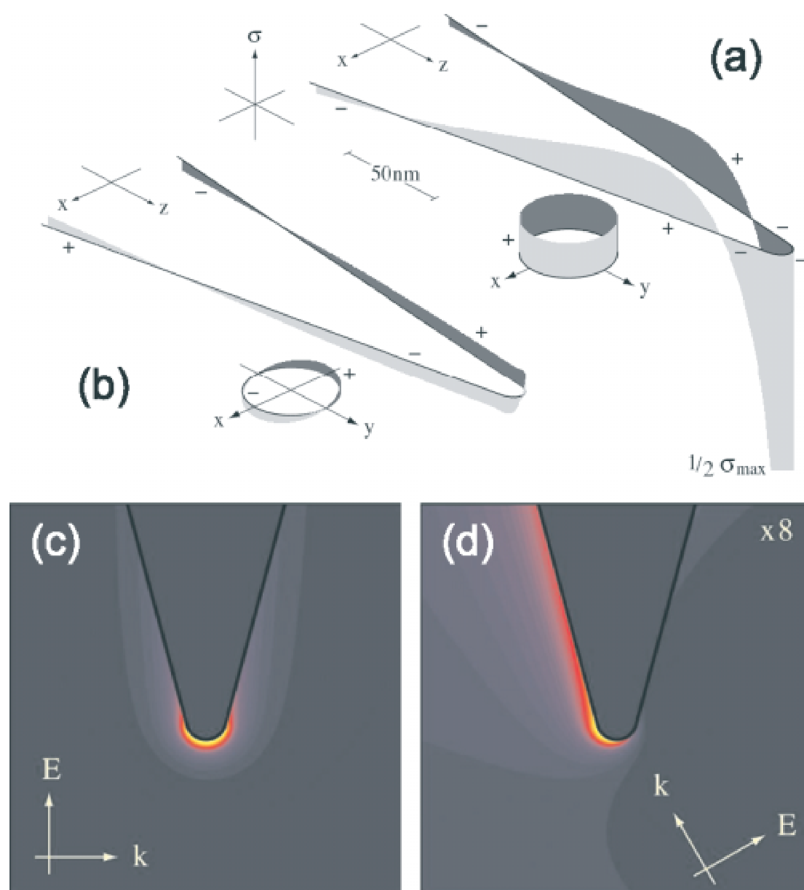

Figure 2. Induced surface charge density at the surface of a sharp metal tip. In (a) the driving field is parallel to the tip shaft, whereas in (b) they are perpendicular to each other. In (a) there is a large surface charge accumulation at the foremost part, responsible for the field enhancement. In (b) the surface charge has a node at the end of the tip.[11] (c) Calculated field distribution at a sharp Au tip for an incident electric field vector parallel to the tip shaft. The graphic shows the localization of the electric field at the tip apex. (d) Field distribution for an incident electric field orientated nonparallel to the tip shaft. The field is no longer confined to the tip apex.

proportional to the intensity of the incident light. Therefore, the total enhancement of the intensity of the scattered light will be given by the product[19,22]

$$M = f(\omega_i)^2 f(\omega_s)^2 \sim f(\omega_i)^4 \quad (5)$$

where we have taken $\omega_v \ll \omega_i \sim \omega_s$. Equation (5) tells us that the total enhancement of the Raman intensity in a TERS experiment is proportional to the fourth power of the electric field enhancement.

As a final comment, it should be noticed that no charges can be accumulated at the tip end if the driving field is polarized transverse to the tip axis, and hence no field enhancement is observed (see Fig. 2(b) and (d)).[19,22] It means that if the incident field is not polarized along the tip axis, only the scattered light can be effectively enhanced, and the maximum enhancement for the Raman intensity will be given by $M = f(\omega_s)^2$. Therefore, it is worth using a mode converter in order to produce a radially symmetric (doughnut) mode, thereby increasing the strength of the longitudinal field components that provide the necessary polarization condition for driving the field enhancement effect. For that, the tip must be positioned at the center of the focus where the longitudinal field lobe is located.[19,22]

Alternatively, linearly polarized beams can also be used if the tip is slightly displaced from the center of the beam into one of the two longitudinal field lobes characteristic of strongly focused Gaussian beams. However, the longitudinal lobes in this case are several times weaker than for doughnut modes.[19,22]

Experimental Setup

The tip-enhanced Raman setup is based on an inverted optical microscope equipped with an x,y-scan stage for raster-scanning a sample sitting on the top of a transparent substrate (Fig. 3). A high numerical aperture objective (1.4 NA) is used to focus a radially polarized laser beam on the substrate surface. A sharp gold tip (Fig. 4) is positioned in the focus of the incident laser beam. The tip is attached to a quartz tuning fork, and it is kept at a distance of ~2 nm from the sample surface by means of a sensitive shear-force feedback mechanism.[24] The scattered light is collected by the same objective (backscattering geometry) and then detected by a single-photon counting avalanche photodiode (APD), or by a combination of a spectrograph and a cooled charge-coupled device (CCD). In the first case (detection by the APD), the scattered beam goes through a low-pass filter and also through a narrow band-pass filter, in order to remove the Rayleigh component and select the wavelength range of interest. When the signal is detected by the CCD, the scattered beam is filtered by a notch filter which removes the Rayleigh scattered

 Copyright © 2009 John Wiley & Sons, Ltd.

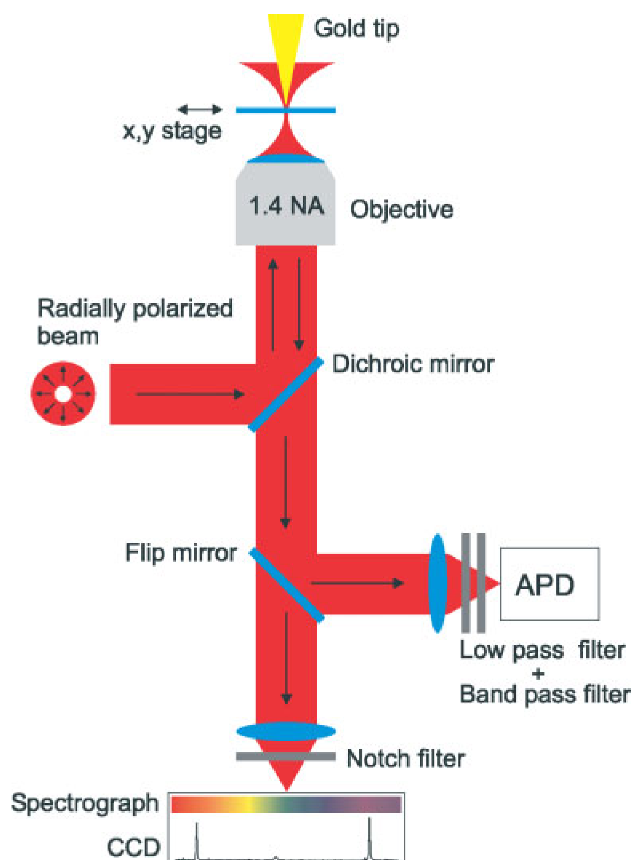

Figure 3. Schematic of the tip-enhanced Raman setup. A sharp gold tip is scanned through a strongly focused laser beam. The optical signal is detected either by an avalanche photodiode (APD) or by a combination of a spectrograph and a CCD.

light. In both cases, the tip-enhanced Raman image is obtained simultaneously with the topographic image by raster-scanning the sample.

Results and Discussion

Figure 5(a) and 5(b) show simultaneously acquired topographic and tip-enhanced Raman images, respectively, of a carbon nanotube bundle on glass. The sample was produced by the arc-discharge method.[1] A linearly polarized Gaussian beam with wavelength 632.8 nm was used as excitation source. The Raman image was detected by integrating the G band intensity around 700 nm (according to the red-shift of ~70 nm from the incident laser wavelength) using an APD. The accumulation time for each image pixel was 10 ms. Figure 5(c) shows the height profile taken along the blue line on the topographic image shown in Fig. 5(a). From this graphic, we find that the diameters of the nanotube bundle and the tip apex are ~2.5 and ~20 nm, respectively. Figure 5(d) shows the intensity profile obtained along the blue line on the tip-enhanced Raman image shown in panel (b). The intensity profile shows the near-field signal with an optical resolution of ~18 nm. This value is close to the diameter of the tip apex obtained from the height profile shown in panel (c). The blue line in Fig. 5(d) is a Gaussian fit for the far-field background. The full width at half-maximum of this Gaussian profile is 290 nm, indicating the diffraction limit for the spatial resolution in the far-field regime.

Figure 5(e) shows the Raman spectra of the nanotube bundle shown in panels (a) and (b) in the presence of the tip (red curve) and without the tip (black curve). The spectra were obtained using the spectrograph/CCD set. The vertical lines delimit the spectral window in which the image shown in panel (b) was obtained. From the value of the RBM wavenumber ($\omega_{\mathrm{RBM}} = 245\ \mathrm{cm}^{-1}$), we can conclude that these Raman spectra are originating from a (10, 3) semiconductor SWNT, whose energy gap for the second optical transition E_{22} is in resonance with the incident laser energy.[2,3] The values for the integrated intensities of the G band were found to be 5.9×10^5 and 1.2×10^5 counts.cm^{-1} for the spectra with and without the tip, respectively.

In order to evaluate the effective enhancement factor for the G band intensity, we should take into account the different areas probed by the near field and the far field.[19,22] Since the nanotube has a larger length than the focus area, we can calculate the area probed by the far-field component as the product of the tube diameter (~2.5 nm) and the focus diameter (~290 nm), which will be 725 nm^2. For the near-field component, the area will be defined by the product of the tube diameter and the tip apex diameter (~18 nm). Then, we can normalize the measured intensities of the G band using the ratio of the respective detected areas, and the result yields an enhancement factor of M ~14. As discussed in the last section, the enhancement factor of the Raman intensity is proportional to the fourth power of the field enhancement (see Eqn 5). Therefore, for the near-field data shown in Fig. 5, we can conclude that the enhanced local field is about two times stronger than the incident field.

Figure 6(a) shows another tip-enhanced Raman image of a HIPco nanotube. A radially polarized (doughnut) mode with wavelength 785 nm was used as excitation source. The Raman image was detected using the APD by integrating the G band intensity around 890 nm. The inset shows the intensity profile taken along the blue line crossing the nanotube, indicating a spatial resolution of ~15 nm. It can be seen from Fig. 6(a) that the far-field background is below the noise level and can barely be observed. This is an indication of a strong field enhancement, resulting from the combination of a radially polarized mode used as excitation source with a properly working tip.

Figure 6(b) shows the Raman spectra of the nanotube shown in part (a) obtained in the presence of the tip (red curve) and without it (black curve). The spectra show the RBM with wavenumber $\omega_{\mathrm{RBM}} = 206\ \mathrm{cm}^{-1}$, indicating that this tube might be a (9,8) semiconductor SWNT.[2,3] The normalized enhancement factor for the G band intensity in this case was found to be M ~770, which leads to a local field enhancement on the order of ~5.

Advances on the Science of Carbon Nanotubes Mediated by TERS

First high-resolution tip-enhanced Raman images of SWNTs

In 2003, Hartschuh *et al*. have shown for the first time tip-enhanced Raman images of SWNTs with spatial resolution better than 30 nm.[16] For that, the authors used sharp silver tips as near-field probes. The high resolution achieved in these experiments made it possible to resolve local variations in the Raman spectrum along an isolated SWNT, which would otherwise be hidden in far-field measurements. The chemical specificity of the near-field Raman method was used to distinguish between SWNTs and humidity-related water contaminations on the sample surface. The near-field

 Copyright © 2009 John Wiley & Sons, Ltd.

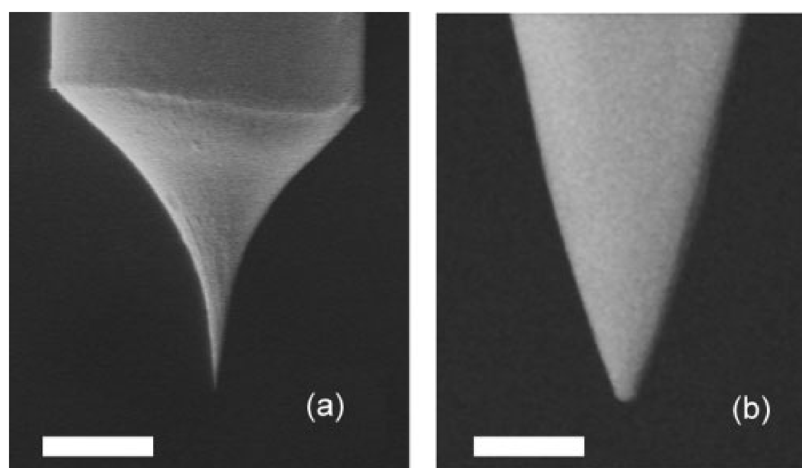

Figure 4. (a) Scanning electron microscopy (SEM) image of a sharp gold tip produced by electrochemical etching. (b) Close-up of the apex of the tip shown in panel (a). The tip radius is about 20 nm at the apex. The scale bar sizes are 40 µm and 100 nm for parts (a) and (b), respectively.

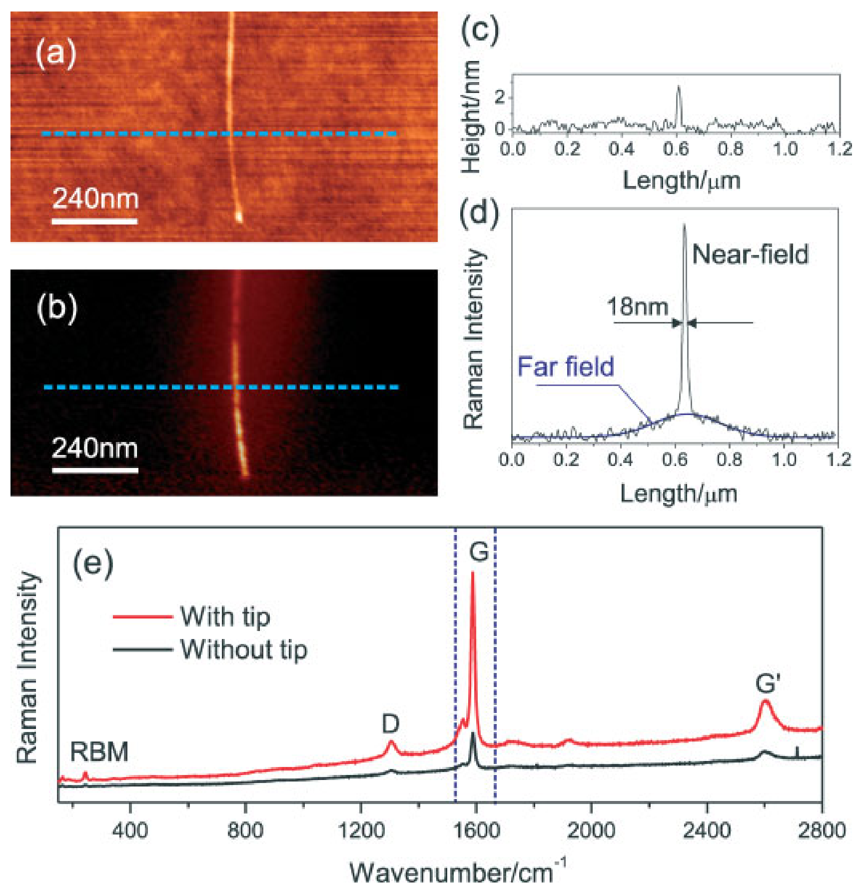

Figure 5. Simultaneously acquired topographic (a) and tip-enhanced Raman (b) images of a carbon nanotube bundle on glass. For the Raman image, a linearly polarized Gaussian beam with wavelength 632.8 nm was used as excitation source. (c) Height profile taken along the blue line on the topographic image shown in part (a). (d)Intensity profile obtained along the blue line on the tip-enhanced Raman image shown in panel (b). (e)Raman spectra of the nanotube bundle shown in panels (a) and (b) in the presence of the tip (red curve) and without the tip (black curve).

origin of the Raman enhancement was proven by tip–sample distance measurements. The authors also observed that the near-field Raman intensity was not sensitive to the polarization direction of the incident laser beam relative to the nanotube axis, showing that the enhanced field is radially symmetric with respect to the tip axis.

Study of localized vibrational modes in SWNTs

Anderson and collaborators[17] have shown the near-field Raman study of localized vibrational modes along individual SWNTs with a spatial resolution of 10–20 nm. The acquisition of spectroscopic information along defective SWNTs grown by the arc-discharge method allowed the authors to detect spatial localization of the

Copyright © 2009 John Wiley & Sons, Ltd.

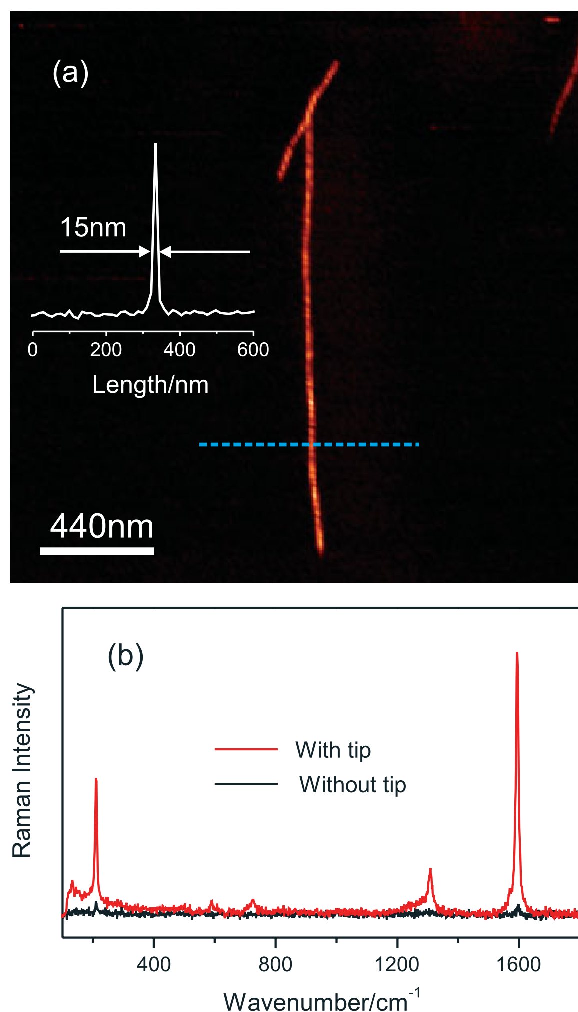

Figure 6. (a) Tip-enhanced Raman image of a HIPco nanotube relative to the G band intensity. A radially polarized (doughnut) mode with wavelength 785 nm was used as excitation source. The inset shows the intensity profile taken along the blue line. (b) Raman spectra of the nanotube shown in part (a) obtained in the presence of the tip (red curve) and without it (black curve).

RBM and the intermediate frequency modes (IFMs) occurring at 600–1100 cm^{-1}.[25] The authors attributed these observations to local changes in the tube structure. They did not observe such localization in the Raman spectra obtained from SWNTs grown by the chemical vapor deposition (CVD) method, where the density of defects leading to structural changes is indeed much lower.

Chirality changes in SWNTs

Reference[18] reports the direct measurement of chirality changes in carbon nanotubes by detecting local changes in the RBM frequency with spatial resolution of 40 nm. For that, the authors used TERS. They observed transitions from semiconductor to metal and from metal to metal by mapping two resonant RBM phonon frequencies along spatially isolated SWNTs. Variations on the G band line shape supported their conclusions. These structures are highly quoted for technological application as intramolecular junctions working as nanoscale diodes and rectifies,[1] and this work clearly show that TERS is a very promising technique to be applied to the characterization of such systems.

Detection of dopants in SWNTs

Maciel *et al*. have shown recently the use of tip-enhanced Raman and tip-enhanced photoluminescence to spatially resolve local charged defects along individual SWNTs.[6] The authors observed a high degree of spatial localization of the photoluminescence emission along the SWNT, and showed that the defect-induced Raman D band has a stronger signal at the same local sites. Based on this coincidence, the authors suggested that the high localization of the photoluminescence signal was related to trapped excitons. They also observed the presence of a new peak in the G′ band in the Raman spectra obtained from those defect sites. The authors have shown that this new peak can be shifted to lower or higher frequencies relative to the frequency of the G′ peak observed in the Raman spectra of pristine tubes. They also observed that this additional G′ peak originates from the presence of charged defects (dopants), having its frequency up/downshifted for p/n dopants. This phenomena was explained by considering the fact that charged defects deform the electron and phonon energy dispersions of carbon nanotubes.

Conclusions

This paper presents the principles of TERS, followed by its applications to the science of carbon nanotubes. It has been shown that the spatial resolution of standard optical microscopy is limited by diffraction to roughly $\lambda/2$. This limit originates from the fact that evanescent field components cannot be detected in the far zone. By placing an optical antenna (metal tip) sufficiently near the sample, we provide a channel through which those near-field components become propagating waves accessible in the far-field regime. The spatial resolution of TERS is given by the diameter of the tip apex, leading to values up to $\lambda/60$. This technique is applied to obtain Raman images of carbon nanotubes with high spatial resolution mediated by local enhancement of the incident and scattered fields. The technique has proved to be a valuable tool for studying structural and electronic properties of carbon nanotubes.

Acknowledgements

This work is financially supported by the Department of Energy (grant DE-FG02-05ER46207).

References

[1] A. Jorio, M. S. Dresselhaus, G. Dresselhaus, *Carbon Nanotubes: Advanced Topics in Synthesis, Properties, and Applications*, *Topics in Applied Physics*, Vol. 111, Springer: Berlin, **2008**.
[2] A. Jorio, R. Saito, J. H. Hafner, C. M. Lieber, M. Hunter, T. McClure, G. Dresselhaus, M. S. Dresselhaus, *Phys. Rev. Lett.* **2001**, *86*, 1118.
[3] P. T. Araujo, I. O. Maciel, P. B. C. Pesce, M. A. Pimenta, S. K. Doorn, H. Qian, A. Hartschuh, M. Steiner, L. Grigorian, K. Hata, A. Jorio, *Phys. Rev. B* **2008**, *77*, 241403.
[4] J. Maultzsch, S. Reich, and C. Thomsen, *Phys. Rev. B* **2001**, *64*, 121 407.
[5] S. Piscanec, M. Lazzeri, J. Robertson, A. C. Ferrari, F. Mauri, *Phys. Rev. B* **2007**, *75*, 035 427.
[6] I. O. Maciel, N. Anderson, M. A. Pimenta, A. Hartschuh, H. Qian, M. Terrones, H. Terrones, J. Campos-Delgado, A. M. Rao, L. Novotny, A. Jorio, *Nat. Mat.* **2008**, *7*, 878.
[7] S. Picanec, M. Lazzeri, F. Mauri, A. C. Ferrari, J. Robertson, *Phys. Rev. Lett.* **2004**, *93*, 185 503.
[8] G. G. Samsonidze, E. B. Barros, R. Saito, J. Jiang, G. Dresselhaus, M. S. Dresselhaus, *Phys. Rev. B* **2007**, *75*, 155 420.

 Copyright © 2009 John Wiley & Sons, Ltd.

[9] S. Pisana, M. Lazzeri, C. Casiraghi, Kostya. S. Novoselov, A. K. Geim, A. C. Ferrari, and F. Mauri, *Nat. Mat.* **2007**, *6*, 198.

[10] R. H. Baughman, A. A. Zakhidov, W. A. de Heer, *Science* **2002**, *297*, 5582.

[11] N. Anderson, A., Hartschuh, L. Novotny, *Mat. Today* **2005**, *8*(5), 50.

[12] A. Hartschuh, *Angew. Chem. Int. Ed.* **2008**, *47*, 8178.

[13] T. Yano, Y. Inouye, S. Kawata, *Nano Lett.* **2006**, *6*, 1269.

[14] T. Yano, P. Verma, S. Kawata, Y. Inouye. *Appl. Phys. Lett.* **2006**, *88*, 093 125.

[15] S. S. Kharintsev, G. G. Hoffmann, P. S. Dorozhkin, G. de With, and J. Loos. *Nanotechnology* **2007**, *18*, 315 502.

[16] A. Hartschuh, E. J. Sánchez, X. S. Xie, L. Novotny, *Phys. Rev. Lett.* **2003**, *90*, 095 503.

[17] N. Anderson, A. Hartschuh, L. Novotny, *J. Am. Chem. Soc* **2005**, *127*, 2533.

[18] N. Anderson, A. Hartschuh, L. Novotny, *Nano Lett.* **2007**, *7*, 577.

[19] L. Novotny and B. Hecht, *Principles of Nano-Optics*, Cambridge University Press, New York, USA, **2006**.

[20] M. Born, and E. Wolf, *Principles of Optics* (6th edn), Pergamon: Oxford, **1970**.

[21] L. Novotny, S. J. Stranick, *Ann. Rev. Phys. Chem.* **2006**, *57*, 303.

[22] A. Hartschuh, M. R. Beverluis, A. Bouhelier, L. Novotny, *Phil. Trans. R. Soc. Lond. A* **2004**, *362*, 807.

[23] W. Hayes, R. Loudon, *Scattering of Light by Crystals*, John Wiley & Sons, New York, USA, **1978**.

[24] K. Karrai, R. D. Grober, *Appl. Phys. Lett.* **1995**, *66*, 1842.

[25] C. Fantini, A. Jorio, M. Souza, L. O. Ladeira, A. G. Souza Filho, R. Saito, Ge. G. Samsonidze, G. Dresselhaus, M. S. Dresselhaus, M. A. Pimenta, *Phys. Rev. Lett.* **2004**, *93*, 087401.

Copyright © 2009 John Wiley & Sons, Ltd.